

Kepler Predictor—Corrector Algorithm: Scattering Dynamics with One-Over-R Singular Potentials

Andreas Markmann,^{*,†} Frank Graziani,[‡] and Victor S. Batista^{*,†}

[†]Department of Chemistry, Yale University, P.O. Box 208107, New Haven, Connecticut 06520-8107, United States

[‡]Center for Applied Scientific Computing and B-Division, Lawrence Livermore National Laboratory, P.O. Box 808, Livermore, California, United States

ABSTRACT: An accurate and efficient algorithm for dynamics simulations of particles with attractive $1/r$ singular potentials is introduced. The method is applied to semiclassical dynamics simulations of electron–proton scattering processes in the Wigner-transform time-dependent picture, showing excellent agreement with full quantum dynamics calculations. Rather than avoiding the singularity problem by using a pseudopotential, the algorithm predicts the outcome of close-encounter two-body collisions for the true $1/r$ potential by solving the Kepler problem analytically and corrects the trajectory for multiscattering with other particles in the system by using standard numerical techniques (e.g., velocity Verlet, or Gear Predictor corrector algorithms). The resulting integration is time-reversal symmetric and can be applied to the general multibody dynamics problem featuring close encounters as occur in electron–ion scattering events, in particle–antiparticle dynamics, as well as in classical simulations of charged interstellar gas dynamics and gravitational celestial mechanics.

1. INTRODUCTION

Understanding the dynamics of particles mutually attracted by $1/r$ singular potentials is a problem common to a wide range of systems in chemistry, biology, physics, and astronomy, including classical and semiclassical studies of electron transfer,¹ excess electrons in liquids,^{2,3} ionic states,⁴ electron scattering and trapping in ionic liquids or solids,^{5–7} attractive plasmas with nuclei and electrons,^{8,9} particle–antiparticle dynamics,¹⁰ dynamics of charged interstellar gas particles,¹¹ and celestial mechanics.^{12,13} However, serious numerical problems typically arise in classical and semiclassical simulations when particles gravitate into each other and the potential gradients (or accelerations) diverge. To avoid this type of Coulomb (or gravitational) catastrophe problem, simulation studies often rely on pseudopotentials where the essential singularities of the potentials are artificially removed. Such approximations lead to integration methods that are both practical and useful for simulations of scattering events with large impact parameters, as typically observed in low-energy collisions of particles with repulsive cores. However, close-encounter collisions are beyond the capabilities of pseudopotential methods, and more rigorous methodologies have to be employed. This paper introduces a predictor–corrector algorithm for dynamics simulations of particles evolving on attractive $1/r$ singular potentials. The method is rigorous and efficient, even when modeling close-encounter collisions. Its application to semiclassical dynamics simulations of electron–proton scattering in the Wigner-transform time-dependent picture shows excellent agreement with full quantum dynamics calculations.

The Coulomb catastrophe problem could be avoided by using a quantum treatment of the attractive interaction, setting a lower limit for the bound state in the potential. However, quantum dynamics methods are computationally demanding and scale poorly (i.e., exponentially) with the number of strongly coupled

particles in the system. For example, quantum dynamics simulations of dense proton plasmas with electrons are usually computationally impractical. Accurate simulations of such systems thus require a rigorous solution to the Coulomb catastrophe problem within the framework of linear scaling particle simulation techniques, analogous to standard molecular dynamics simulations. When implemented with adaptive time-step integrators, such methods are capable of accurately simulating point particles interacting through singular attractive pair potentials, bypassing energy conservation problems associated with divergent accelerations.

Adaptive time-step integrators are the most common techniques applied to ensure energy conservation for systems with rapidly changing potential gradients (or accelerations). However, such methods are hopeless for simulations of close encounters since the integration time-steps converge to zero as the accelerations diverge and bring the simulation to a halt. [Specifically, the time step becomes so small that additive terms that include the time step as a factor become smaller than the least significant digit of the coordinate, so coordinates no longer evolve.] This happens even if individual time-steps are used for each particle.^{12,14} Conversely, imposing a minimal time-step yields trajectories that eventually violate energy conservation, prompting the common practice of using pseudopotentials to artificially remove the singularities and ensure energy conservation.

Smoothed (pseudo)potentials with a finite value at the origin have been postulated for electron dynamics^{5,8} as well as for ion dynamics¹⁵ and astrophysical simulations.^{12,16} The Coulomb potential is also commonly switched-off at small interparticle distances through the use of switching functions (e.g., the error function).^{7,9} These cases are typically distinguished from the

Received: June 29, 2011

Published: November 08, 2011

construction of pseudopotentials based on physical insights, such as the screening effect of electrons in the conduction band of metals.⁶ In ionic solids (e.g., alkali halides, oxide insulators, or semiconductors), however, there are no electrons in the conduction band that could offer screening of Coulombic interactions. Therefore, alternative methods are required.

Changes in the potential usually alter the underlying dynamics of the systems yielding artificial effects that disappear only when the pseudopotentials become more and more similar to the true potentials. In that limit, however, the numerical problems due to large gradients usually reappear. An approach that avoids changing the singular potential has been developed for gravitational systems, implementing a change of variables that regularizes the dynamics (e.g., the Kustaanheimo–Stiefel (KS) regularization and related methods^{12,17–21}) and applies standard numerical integration for the new variables rather than for the original coordinates. This requires transformation of the time variable and coordinates that depend on the interparticle distance for the pair of particles experiencing a close encounter. Great care must be taken to keep track of transformations for multiple close encounters and to match up time-steps so that the interaction with other particles present in the simulation is properly accounted for, while not sacrificing efficiency.^{20,21} As a consequence of these complications, the method is, to our knowledge, implemented in only a few stellar codes.²²

In this paper, we introduce a simple Kepler predictor corrector (KPC) algorithm where close-encounter collisions are integrated analytically by solving the Kepler two-body problem without altering (or smoothing) the Coulomb potential and updating coordinates based on the residual potential due to particles not participating in the close encounter. A simple well-known example for such an approach is the lightly damped harmonic oscillator, where the frequency of the resulting oscillation is approximately the same as that of the underlying undamped oscillator and only the amplitude may be viewed as modulated.²³ In molecular dynamics, the analytic solution of the harmonic oscillator has been employed by splitting linear molecule Hamiltonians into a harmonic and anharmonic part and treating high frequency components of the molecular vibrations analytically, while treating low frequency components numerically.^{24–29} In biological systems, a large speedup was achieved by treating water molecules as rigid and using analytic solutions for their motion.³⁰

For the $1/r$ problem, an update scheme based on a single momentum shift has been proposed previously for the purpose of simulating ion collisions.³¹ We propose a method that corrects the predicted scattering trajectories with an additional term rigorously derived from numerical integrators (e.g., velocity Verlet or Gear Predictor Corrector algorithms), accounting for the regular influence of other particles (or external fields) in the system. The integration method as a whole is time-reversal symmetric, does not require any time-variable transformation, and can be applied to the general multibody dynamics problem with close encounters, as in electron–proton scattering processes, particle–antiparticle dynamics, and charged gas dynamics. Algorithmically, the complete potential is separated into two parts, including an integrable two-body term that is dominant at close encounters and a correction due to interactions with all other particles (or potentials) in the system. With an integrable two-body problem (as is the case of Coulombic $1/r$ or van der Waals $1/r^6$ potentials),³² the analytic solution of close encounters is employed, and the effect due to interactions with all other particles is introduced by augmenting the analytic solution with

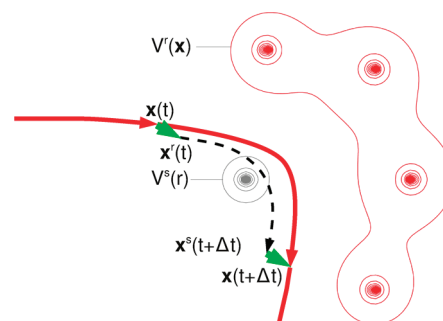


Figure 1. KPC trajectory (red line) of a particle scattered by a singularity $V^s(r)$, obtained by solving the Kepler problem (dashed line), taking into account the effect of a weakly varying residual potential $V^r(r)$ (bold green lines) as described in the text.

additional terms that stem from the numerical integrator (e.g., the velocity Verlet method^{33,34}). The resulting KPC method allows for integration time-steps on the same order as used for regular potentials and hence reduces the numerical effort for problems with close encounters. It is applicable for any integrable singular pair potential,³² including the family of integrable spherically symmetric singular pair potentials that are the focus of this paper.

The paper is organized as follows. Section 2 introduces the KPC method as applied to modeling the dynamics of a particle evolving on a potential with multiple singularities and its generalization to multibody dynamics. Section 3 describes its implementation for semiclassical simulations of electron–proton scattering in the Wigner-transform time-dependent picture. Section 4 presents concluding remarks in perspective of the KPC limitations and applicability as a general method.

2. KEPLER PREDICTOR CORRECTOR ALGORITHM

2.1. Single Particle Colliding with Multiple Singularities.

Consider the general case of a single particle moving in a stationary potential with multiple singularities, as shown in Figure 1. The total potential V acting on the particle is composed of the spherically symmetric potential V^s with the singularity nearest to the particle, and the residual potential V^r :

$$V(\mathbf{x}) = V^s(r) + V^r(\mathbf{x}) \quad (1)$$

As an example, we consider the semiclassical trajectory of a fast electron undergoing multiple scattering through proton plasma, under the Born–Oppenheimer approximation, where $V(\mathbf{x})$ is defined as the Coulomb potential due to the closest proton $V^s(\mathbf{x})$ plus the sum of Coulomb potentials $V^r(\mathbf{x})$ due to the other protons in the plasma.

During a close encounter with the singularity $V^s(r)$, the electron scattering force is dominated by this closest proton, and accurate numerical integration faces several difficulties, including the following:

1. the large absolute value of potential energy,
2. the very large norm of the potential gradient and higher derivatives, and hence,
3. the very large acceleration of particles and curvature of trajectories,
4. the requirement of very small time-steps of standard integrators (such as the Verlet methods and the Nordsieck–Gear Predictor–Corrector methods^{33,34}).

The KPC algorithm addresses these challenges by first predicting the coordinates and momenta due to the collision with the closest singularity $V^s(r)$ and then correcting the resulting coordinates and momenta according to the residual term, as follows.

Formally, $\mathbf{x}(t)$ and $\mathbf{p}(t)$ are obtained according to the velocity Verlet method:^{33–35}

$$\mathbf{x}(t + \Delta t) = \mathbf{x}(t) + \frac{\Delta t}{m} \mathbf{p}(t) - \frac{\Delta t^2}{2m} \nabla V|_{\mathbf{x}(t)} \quad (2)$$

$$\mathbf{p}(t + \Delta t) = \mathbf{p}(t) - \frac{\Delta t}{2} (\nabla V|_{\mathbf{x}(t)} + \nabla V|_{\mathbf{x}(t+\Delta t)}) \quad (3)$$

where $m = m_e$ is the mass of the particle, and the time increment Δt is assumed to be sufficiently short to ensure energy conservation. However, to address the numerical challenge of the close encounter, we decompose the total force ∇V into the contribution due to the nearest singularity ∇V^s and the contributions due to smaller residual forces ∇V^r and write suggestively:

$$\mathbf{x}(t + \Delta t) = \mathbf{x}(t) + \frac{\Delta t}{m} \mathbf{p}(t) - \frac{\Delta t^2}{2m} (\nabla V^s|_{\mathbf{x}(t)} + \nabla V^r|_{\mathbf{x}(t)}) \quad (4)$$

$$\begin{aligned} \mathbf{p}(t + \Delta t) = \mathbf{p}(t) - \frac{\Delta t}{2} (\nabla V^r|_{\mathbf{x}(t)} + \nabla V^s|_{\mathbf{x}(t)} \\ + \nabla V^s|_{\mathbf{x}(t+\Delta t)} + \nabla V^r|_{\mathbf{x}(t+\Delta t)}) \end{aligned} \quad (5)$$

and introducing auxiliary coordinates

$$\mathbf{x}^r(t) = \mathbf{x}(t) \quad (6)$$

$$\mathbf{p}^r(t) = \mathbf{p}(t) - \frac{\Delta t}{2} \nabla V^r|_{\mathbf{x}(t)} \quad (7)$$

$$\mathbf{x}^s(t + \Delta t) = \mathbf{x}^r(t) + \frac{\Delta t}{m} \mathbf{p}^r(t) - \frac{\Delta t^2}{2m} \nabla V^s|_{\mathbf{x}^r(t)} \quad (8)$$

$$= \mathbf{x}(t) + \frac{\Delta t}{m} \mathbf{p}(t) - \frac{\Delta t^2}{2m} (\nabla V^s|_{\mathbf{x}(t)} + \nabla V^r|_{\mathbf{x}(t)}) \quad (9)$$

$$\mathbf{p}^s(t + \Delta t) = \mathbf{p}^r(t) - \frac{\Delta t}{2} (\nabla V^s|_{\mathbf{x}^r(t)} + \nabla V^s|_{\mathbf{x}^s(t+\Delta t)}) \quad (10)$$

We obtain by comparison with eqs 4 and 5:

$$\mathbf{x}(t + \Delta t) = \mathbf{x}^s(t + \Delta t) \quad (11)$$

$$\mathbf{p}(t + \Delta t) = \mathbf{p}^s(t + \Delta t) - \frac{\Delta t}{2} \nabla V^r|_{\mathbf{x}(t+\Delta t)} \quad (12)$$

The auxiliary variables were constructed such that eqs 8 and 10 become velocity Verlet equations for only the singular potential $V^s(r)$, so they provide a practical way of predicting coordinates and momenta at time $t + \Delta t$, as solely determined by the two-body collision with the closest proton. During a close encounter, however, such equations become numerically stiff, and they are replaced by analytic solutions of the corresponding two-body Kepler initial value problem with initial coordinates $(\mathbf{x}^r(t), \mathbf{p}^r(t))$

[three-body collisions are usually prevented by Coulombic repulsion under cool plasma conditions] as described in section 2.3. [The two-body problem is integrable for a variety of spherically symmetric interaction potentials, including the Coulomb r^{-1} potential and van der Waals r^{-6} type potentials.³² In particular, the two-body problem for the $1/r$ potential is known as the “Kepler problem,” since the elliptical trajectories obey Kepler’s laws of planetary motion.] Having obtained $\mathbf{x}^s(t + \Delta t)$ and $\mathbf{p}^s(t + \Delta t)$, we obtain $\mathbf{x}(t + \Delta t)$ and $\mathbf{p}(t + \Delta t)$ by correcting the predicted coordinates and momenta according to eq 12. It turns out that $\mathbf{x}^r(t)$ and $\mathbf{x}^s(t + \Delta t)$ are not, as indicated in Figure 1, distinct from $\mathbf{x}(t)$ and $\mathbf{x}(t + \Delta t)$, but their corresponding momenta are.

The resulting KPC algorithm thus allows for the integration of close-encounter collisions beyond the capabilities of the standard velocity Verlet algorithm (i.e., eqs 4 and 5), as follows:

- A. Determine $\mathbf{p}^r(t)$ by a momentum shift according to eq 6.
- B. Obtain $(\mathbf{x}^s(t + \Delta t), \mathbf{p}^s(t + \Delta t))$ by solving the two-body Kepler problem. The analytic solution \mathbf{S}^K is a set that contains position, momentum, and, in principle, all higher derivatives of the position at the final time $t + \Delta t$:

$$(\mathbf{x}^s(t + \Delta t), \mathbf{p}^s(t + \Delta t)) \subset \mathbf{S}^K(\mathbf{x}^r(t), \mathbf{p}^r(t)) \quad (13)$$

- C. From $\mathbf{p}^s(t + \Delta t)$, determine $\mathbf{p}(t + \Delta t)$ according to eq 12.

Maximum efficiency is achieved when the analytic task is restricted to small regions surrounding the singularity closest to the scattering particle, since the solution of the Kepler problem is more involved than a velocity Verlet integration step. This is typically ensured by defining a cutoff distance r_{\min} from the singularity center, below which the KPC method is implemented. In the case under consideration, the potential is stationary, and the cutoff distance can be set to a constant value much smaller than half the minimal distance between singularities, $r_{\min} \ll 1/2 \min\{r_{ij}\}$. It should be small enough that the residual potential V^r is always much more slowly varying than the close-encounter potential V^s , guaranteeing that the singular potential dominates the dynamics and the influence of the residual potential leads only to small corrections. To make the method fully time-reversal symmetric, the cutoff criterion has to be made time-reversal symmetric as well, in the following way. The KPC method is used when the initial coordinate is inside the cutoff radius from a scattering center. If the coordinate after the time step is outside the cutoff radius, the result is discarded, and a velocity Verlet step is made instead.

In contrast to ref 31 where a single momentum shift was applied, our symmetrized approach uses two momentum shifts per time step. However, the potential gradient needs only be evaluated once per time step.

2.2. Multibody Molecular Dynamics. The generalization of the KPC algorithm, introduced in section 2.1, to multibody molecular dynamics is straightforward. Let $(\mathbf{x}(t), \xi(t))$ and $(\mathbf{p}(t), \pi(t))$ be the position and momentum vectors of the system at time t . Without a loss of generality, let $(\mathbf{x}(t), \mathbf{p}(t))$ be the six-dimensional phase-space vector describing the relative motion of two particles undergoing a close encounter and m be their reduced mass, while their center-of-mass coordinate, along with the coordinates of all other particles (some of which may also be in a close encounter), is contained in the phase-space vector $(\xi(t), \pi(t))$.

While the interparticle potential $V(\mathbf{x}(t), \xi(t))$ includes all of the interactions, only the dynamics of the relative coordinate

$(\mathbf{x}(t), \mathbf{p}(t))$ are discussed in the following. Accordingly, the gradient will denote the vector of partial derivatives with respect to the relative coordinate \mathbf{x} only:

$$\nabla_3 V = \left(\frac{\partial V}{\partial x_1}, \dots, \frac{\partial V}{\partial x_3} \right) \quad (14)$$

The dependence of the phase-space relative coordinates $(\mathbf{x}(\Delta t), \mathbf{p}(\Delta t))$ on initial conditions $(\mathbf{x}(0), \mathbf{p}(0))$ is then approximated by

$$\mathbf{x}(t + \Delta t) = \mathbf{x}(t) + \frac{\Delta t}{m} \mathbf{p}(t) - \frac{\Delta t^2}{2m} \nabla_3 V|_{(\mathbf{x}(t), \xi(t))} \quad (15)$$

$$\begin{aligned} \mathbf{p}(t + \Delta t) = & \mathbf{p}(t) - \frac{\Delta t}{2} (\nabla_3 V|_{(\mathbf{x}(t), \xi(t))} \\ & + \nabla_3 V|_{(\mathbf{x}(t+\Delta t), \xi(t+\Delta t))}) \end{aligned} \quad (16)$$

To deal with the close encounter, the potential V is again written as a sum of the close encounter potential $V^s(r)$, $r = \|\mathbf{x}\|$, and the residual potential $V^r(\mathbf{x}, \xi)$:

$$V(\mathbf{x}, \xi) = V^s(r) + V^r(\mathbf{x}, \xi) \quad (17)$$

and eqs 15 and 16 become

$$\begin{aligned} \mathbf{x}(t + \Delta t) = & \mathbf{x}(t) \\ & + \frac{\Delta t}{m} \mathbf{p}(t) - \frac{\Delta t^2}{2m} (\nabla_3 V^s|_{\mathbf{x}(t)} \\ & + \nabla_3 V^r|_{(\mathbf{x}(t), \xi(t))}) \end{aligned} \quad (18)$$

$$\begin{aligned} \mathbf{p}(t + \Delta t) = & \mathbf{p}(t) - \frac{\Delta t}{2} (\nabla_3 V^r|_{(\mathbf{x}(t), \xi(t))} \\ & + \nabla_3 V^s|_{\mathbf{x}(t)} + \nabla_3 V^s|_{\mathbf{x}(t+\Delta t)} \\ & + \nabla_3 V^r|_{(\mathbf{x}(t+\Delta t), \xi(t+\Delta t))}) \end{aligned} \quad (19)$$

Following section 2.1, we define appropriate auxiliary coordinates and momenta:

$$\mathbf{x}^r(t + \Delta t) = \mathbf{x}(t) \quad (20)$$

$$\mathbf{p}^r(t + \Delta t) = \mathbf{p}(t) - \frac{\Delta t}{2} \nabla_3 V^r|_{(\mathbf{x}(t), \xi(t))} \quad (21)$$

$$\mathbf{x}^s(t + \Delta t) = \mathbf{x}^r(t) + \frac{\Delta t}{m} \mathbf{p}^r(t) - \frac{\Delta t^2}{2m} \nabla_3 V^s|_{\mathbf{x}^r(t)} \quad (22)$$

$$\mathbf{p}^s(t + \Delta t) = \mathbf{p}^r(t) - \frac{\Delta t}{2} (\nabla_3 V^s|_{\mathbf{x}^r(t)} + \nabla_3 V^s|_{\mathbf{x}^s(t+\Delta t)}) \quad (23)$$

and we obtain

$$\mathbf{x}(t + \Delta t) = \mathbf{x}^s(t + \Delta t) \quad (24)$$

$$\mathbf{p}(t + \Delta t) = \mathbf{p}^s(t + \Delta t) - \frac{\Delta t}{2} \nabla_3 V^r|_{(\mathbf{x}(t+\Delta t), \xi(t+\Delta t))} \quad (25)$$

During a close encounter, eqs 22 and 23 are replaced by the analytic solution of the Kepler problem, as described in section 2.3, and the resulting values are then augmented according to

eqs 24 and 25. The resulting algorithm for multibody molecular dynamics is summarized, as follows:

1. Determine $\mathbf{p}^r(t)$ by momentum shift according to eq 21.
2. Compute $(\mathbf{x}^s(t + \Delta t), \mathbf{p}^s(t + \Delta t))$ by solving the Kepler problem \mathbf{S}^K :

$$(\mathbf{x}^s(t + \Delta t), \mathbf{p}^s(t + \Delta t)) \subset \mathbf{S}^K(\mathbf{x}(t), \mathbf{p}(t)) \quad (26)$$

3. Obtain coordinates $\mathbf{x}(t + \Delta t)$ and $\xi(t + \Delta t)$, as follows:
 - a. From $\mathbf{x}^s(t + \Delta t)$, determine $\mathbf{x}(t + \Delta t)$ according to eq 24.
 - b. Obtain $\xi(t + \Delta t)$ by using velocity Verlet, or otherwise solving steps 2 and 3a for relative coordinates describing two-body close encounters.
4. Obtain momenta $\mathbf{p}(t + \Delta t)$ and $\mathbf{p}^s(t + \Delta t)$, as follows:
 - a. From $\mathbf{p}^s(t + \Delta t)$, determine $\mathbf{p}(t + \Delta t)$ according to eq 25.
 - b. Determine $\pi(t + \Delta t)$, analogously to step 3b.

2.3. Kepler Problem. When a close encounter is detected, we consider the particle attracted by the nearest singularity:

$$V^s(r) = -\frac{\gamma}{r} \quad (27)$$

where

$$\mathbf{r}(t) = \mathbf{x}^s(t) - \mathbf{X} \quad (28)$$

with \mathbf{X} being the position of the singularity. We solve the equation of motion:

$$\ddot{\mathbf{r}} + \mu \frac{\mathbf{r}}{r^3} = 0 \quad (29)$$

with force parameter $\mu = \gamma/m$ resulting from the gravitational or Coulomb coefficient γ and the mass m , and initial conditions $\mathbf{r}_0 = \mathbf{x}(t) - \mathbf{X}$ and $\mathbf{v}_0 = \dot{\mathbf{x}}(t)$. The solutions exploit the conservation of specific angular momentum $\mathbf{L} = \mathbf{r} \times \mathbf{v}$, specific energy $h^s(t) = \mathbf{v}^2/2 - \mu/r$, and eccentricity vector $\mathbf{e} = \mathbf{v} \times (\mathbf{r} \times \mathbf{v})/\mu - \mathbf{r}/r$.

Equation 29 is regularized by introducing the fictitious time τ with

$$\frac{d}{d\tau} = r \frac{d}{dt} \quad (30)$$

leading to the regularized equation of motion

$$\mathbf{r}'' - 2h^s \mathbf{r} = -\mu \mathbf{e} \quad (31)$$

where the derivatives in eq 31 are in respect to τ , and the initial conditions are modified according to eq 30 to $\mathbf{r}(\tau = 0) = \mathbf{r}_0$ and $\mathbf{r}'(\tau = 0) = r\mathbf{v}_0$. This is a harmonic oscillator problem that is readily solved by exponential functions, typically leading to real solutions that are trigonometric or hyperbolic functions.

The motion is characterized according to four classes of possible solutions, including circular, parabolic, elliptic, and hyperbolic, as shown in the following subsections.³⁶ [In contrast, ref 36 considers 13 classes of solutions, including the circular case and 12 other cases generated from the elliptic, hyperbolic, and parabolic classes as subdivided according to the values of the rotational momentum and fictitious time τ , described below.] The circular and parabolic cases have simple, explicit solutions, while the elliptic and hyperbolic cases lead to Kepler equations that need to be solved iteratively.^{37,38}

2.3.1. Circular Motion. When $\mathbf{r}_0 \cdot \mathbf{v}_0 = 0$, the eccentricity $\mathbf{e} = 0$ and eq 31 becomes homogeneous. In this case, $\mathbf{r}_0 \cdot \mathbf{v}_0 = 0$ and $v_0 = (\mu/r_0)^{1/2}$; i.e., the coordinate change is orthogonal to the

radius vector, so that particle motion is circular and

$$\mathbf{r}(t + \Delta t) = c_r \mathbf{r}_0 + c_v \frac{\mathbf{v}_0}{n} \quad (32)$$

$$\mathbf{v}(t + \Delta t) = -nc_v \mathbf{r}_0 + c_r \mathbf{v}_0 \quad (33)$$

where $c_v = \sin(n(t + \Delta t))$ and $c_r = \cos(n(t + \Delta t))$, with $n = j^3/\mu$ and $j = (2|E^s(t + \Delta t)|/m)^{1/2}$.

2.3.2. *Parabolic Motion*. When $e = 1$, the specific energy $h^s = 0$, and eq 31 has no linear term, giving the parabolic solution

$$\mathbf{r}(t + \Delta t) = \frac{1}{2}(p - \mu[\tau(t + \Delta t)]^2)\mathbf{e} + \tau(t + \Delta t)\mathbf{B} \quad (34)$$

$$r(t + \Delta t) = \frac{1}{2}(p + \mu[\tau(t + \Delta t)]^2) \quad (35)$$

$$\mathbf{v}(t + \Delta t) = \frac{1}{r(t + \Delta t)}(-\mu[\tau(t + \Delta t)]\mathbf{e} + \mathbf{B}) \quad (36)$$

where $\mathbf{B} = \mathbf{L} \times \mathbf{e}$. The *fictitious time* $\tau(t)$, introduced above, is obtained by solving the Kepler equation:

$$t - t_p = \frac{1}{2}\left(p\tau(t) + \frac{\mu}{3}[\tau(t)]^3\right) \quad (37)$$

where t_p is the *pericenter time*:

$$t_p = -\tau_0\left(p + \frac{\mu}{3}\tau_0^2\right) \quad (38)$$

p is the semilatus rectum:

$$p = \frac{\mathbf{L}^2}{\mu} \quad (39)$$

and τ_0 is the fictitious time at time t :

$$\tau_0 = \frac{\mathbf{r}_0 \cdot \mathbf{v}_0}{\mu} \quad (40)$$

Equation 37 can be solved explicitly to obtain the fictitious time, as follows:

$$\tau(t) = \frac{1}{\sqrt[3]{\mu}}(\sqrt[3]{t_D + \sqrt{D}} + \sqrt[3]{t_D - \sqrt{D}}) \quad (41)$$

where negative values are assumed for negative arguments of the cube root, $t_D = 3(t - t_p)$ and $D = t_D^2 + p^3/\mu$.

2.3.3. *Elliptic and Hyperbolic Motion*. When $e \neq 0$ and 1, the motion is either elliptic ($e < 1$, $h^s < 0$) or hyperbolic ($e > 1$, $h^s > 0$). In either case, we obtain the eccentric anomaly:

$$\varepsilon(t + \Delta t) = j\tau(t + \Delta t) \quad (42)$$

as the solution of the (elliptic or hyperbolic) Kepler equation at time $t + \Delta t$, as described below. The resulting eccentricity defines the values of c_v and c_r (see below) and, therefore, the coordinates and velocities, as follows:

$$\mathbf{r}(t + \Delta t) = \frac{1}{k}\left(\frac{c_r}{e} - 1\right)\mathbf{e} + \frac{c_v}{ej}\mathbf{B} \quad (43)$$

$$r(t + \Delta t) = \frac{1 - ec_r}{k} \quad (44)$$

$$\mathbf{v}(t + \Delta t) = \frac{1}{er(t + \Delta t)}\left(-\frac{\mu c_v}{j}\mathbf{e} + c_r\mathbf{B}\right) \quad (45)$$

where $k = -2h^s/\mu$ and $j = (2|h^s|)^{1/2}$.

When $h^s(t) < 0$, the eccentricity ε is the solution of the *elliptic Kepler equation*:

$$n(t + \Delta t - t_p) = \varepsilon(t + \Delta t) - e \sin[\varepsilon(t + \Delta t)] \quad (46)$$

$n = j^3/\mu$, which can be solved iteratively, as described in section 2.3.4. The resulting $\varepsilon(t + \Delta t)$ gives the trigonometric functions:

$$c_v = \sin[\varepsilon(t + \Delta t)] \quad (47)$$

$$c_r = \cos[\varepsilon(t + \Delta t)] \quad (48)$$

which determine the coordinates and velocities, according to eqs 43 and 45.

The pericenter time t_p , introduced by eq 46, is obtained from the eccentricity at the initial time ε_0 , as follows:

$$t_p = -\frac{\varepsilon_0 - e \sin \varepsilon_0}{n} \quad (49)$$

where $\varepsilon_0 = \text{atan2}(y, x)$, with

$$y = \sin \varepsilon_0 = \frac{n}{k\mu e}\mathbf{r}_0 \cdot \mathbf{v}_0 \quad (50)$$

$$x = \cos \varepsilon_0 = \frac{1}{e}\left(1 - \frac{nr_0}{j}\right) \quad (51)$$

Analogously, when $h^s(t) > 0$, the eccentricity $\varepsilon(t + \Delta t)$ is the solution of the *hyperbolic Kepler equation*:

$$n(t + \Delta t - t_p) = -\varepsilon(t + \Delta t) + e \sinh \varepsilon(t + \Delta t) \quad (52)$$

which is solved iteratively, as described in section 2.3.4, using the pericenter time:

$$t_p = \frac{1}{n}\left(\sinh^{-1}\left(-\frac{1}{e} \cdot \frac{n\mathbf{r}_0 \cdot \mathbf{v}_0}{\mu k}\right) + \frac{n\mathbf{r}_0 \cdot \mathbf{v}_0}{\mu k}\right) \quad (52a)$$

The resulting eccentricity $\varepsilon(t + \Delta t)$ gives the hyperbolic functions

$$c_v = \sinh \varepsilon(t + \Delta t) \quad (53)$$

$$c_r = \cosh \varepsilon(t + \Delta t) \quad (54)$$

that determine the coordinates and velocities, according to eqs 43 and 45.

2.3.4. *Iterative Solution of Elliptic and Hyperbolic Equations*. The elliptic and hyperbolic Kepler equations, introduced by eqs 46 and 52, have the general form

$$n(t + \Delta t - t_p) = M = \pm \varepsilon \mp e \sin(h) \varepsilon \quad (55)$$

When $n(t + \Delta t - t_p) < 0$, M is replaced by its absolute value, as follows:

$$|M| = \pm \varepsilon_a \mp e \sin(h) \varepsilon_a \quad (56)$$

Therefore, the solution of eq 55 is

$$\varepsilon(t + \Delta t) = \varepsilon = \text{sgn}(M)\varepsilon_a \quad (57)$$

Equation 56 is solved iteratively,³⁸ starting from an initial guess $\varepsilon_a^{(0)}$ applicable over the whole range of possible parameters

M and e , where each Halley's iteration is followed by a Newton–Raphson optimization. The iterative scheme typically converges to machine accuracy in about three iterations.³⁷ The initial guess $\varepsilon_a^{(0)}$ is obtained, as follows:

Elliptic Kepler Equation. For elliptic motion ($0 \leq M \leq \pi$ and $0 \leq e \leq 1$) and small M , we expand the \sin function in eq 56 to third order, and the resulting approximation of M is substituted in eq 55, giving a cubic approximation of the elliptic Kepler equation:

$$0 = \varepsilon_{00}^3 + 3q\varepsilon_{00} - 2r \quad (58)$$

where $q = 2(1 - e)/e$ and $r = 3M/e$. Solving eq 58, we obtain

$$\varepsilon_{00} = \frac{2r}{c_v^2 + q + (q/w)^2} \quad (59)$$

where $c_v = ((r^2 + q^3)^{1/2} + r)^{1/3}$. On the other hand, for large M , a good initial guess is

$$\varepsilon_{01} = M$$

Therefore, we define an initial guess that is valid for intermediate values of M , as an M -weighted average of the small M guess ε_{00} and the large M guess ε_{01} :

$$\varepsilon_a^{(0)} = \frac{1}{\pi}(M \times \varepsilon_{01} + (\pi - M) \times \varepsilon_{00}) \quad (60)$$

$$= \frac{1}{\pi}(M^2 + (\pi - M) \times \varepsilon_{00}) \quad (61)$$

Hyperbolic Kepler Equation. For hyperbolic motion ($M > 0$ and $1 \leq e$) with small M , the \sinh function in eq 56 is expanded to third order, and the resulting approximation of M is introduced into eq 55 to give the cubic approximation to the hyperbolic Kepler equation:

$$0 = \varepsilon_{00}^3 + 3q\varepsilon_{00} - 2r \quad (62)$$

where $q = 2(e - 1)/e$ and $r = 3M/e$, with the same formal solution introduced by eq 59, although there are different values of q and r .

Bounded coefficients are obtained through an iterative procedure based on the hyperbolic equation divided by e , as follows:

$$0 = -M - \varepsilon + e \sinh[\varepsilon] \quad (63)$$

$$0 = -L - g\varepsilon + \sinh[\varepsilon] \quad (64)$$

with $L = M/e$ and $g = 1/e$. For large L , a good initial guess is

$$\varepsilon_{01} = \sinh^{-1} L \quad (65)$$

which is again mixed with ε_{00} , as follows:

$$\varepsilon_a^{(0)} = \frac{M \times \varepsilon_{01} + 1 \times \varepsilon_{00}}{M + 1} \quad (66)$$

$$= \frac{M \times \sinh^{-1} L + \varepsilon_{00}}{M + 1} \quad (67)$$

3. ELECTRON SCATTERING

3.1. Time-Dependent Wigner Transform. This section illustrates the capabilities of the KPC algorithm, introduced in section 2, as applied to semiclassical dynamics simulations of electron–proton scattering processes in the Wigner-transform

time-dependent picture. Simulations consider the problem of electron scattering from stationary protons, as described within the Born–Oppenheimer approximation (i.e., with $m = m_e$ and the Coulombic parameter $\gamma = 1$ au, so that $\mu = \gamma/m = 1$ au).

The initial state for the scattering electron is defined by the three-dimensional Gaussian:

$$\psi_0(\mathbf{x}) = (2\pi\sigma^2)^{-3/4} \exp\left(-\frac{(\mathbf{x} - \mathbf{x}_0)^2}{4\sigma^2} + \frac{i}{\hbar} \mathbf{p}_0(\mathbf{x} - \mathbf{x}_0)\right) \quad (68)$$

with average position \mathbf{x}_0 and momentum \mathbf{p}_0 . The corresponding Wigner transform:³⁹

$$P_0(\mathbf{x}, \mathbf{p}) = \frac{1}{(2\pi\hbar)^3} \int_{-\infty}^{\infty} \psi_0^*\left(\mathbf{x} + \frac{\mathbf{s}}{2}\right) \psi_0\left(\mathbf{x} - \frac{\mathbf{s}}{2}\right) e^{i\mathbf{p} \cdot \mathbf{s}} d\mathbf{s} \quad (69)$$

$$= \frac{1}{(2\pi\hbar\sigma_x\sigma_p)^3} \exp\left[-\frac{(\mathbf{x} - \mathbf{x}_0)^2}{2\sigma_x^2} - \frac{(\mathbf{p} - \mathbf{p}_0)^2}{2\sigma_p^2}\right] \quad (70)$$

defines the initial phase-space distribution function, where $\sigma_x = \sigma$ and σ_p is defined by the uncertainty relation $\sigma_x\sigma_p = \hbar/2$.

The full quantum-mechanical Wigner distribution $P_t^{\text{QM}}(\mathbf{x}, \mathbf{p})$ is computed as

$$P_t^{\text{QM}}(\mathbf{x}, \mathbf{p}) = \frac{1}{(2\pi\hbar)^3} \int_{-\infty}^{\infty} e^{i/\hbar \mathbf{p} \cdot \mathbf{s}} \psi_t^*\left(\mathbf{x} + \frac{\mathbf{s}}{2}\right) \psi_t\left(\mathbf{x} - \frac{\mathbf{s}}{2}\right) d\mathbf{s} \quad (71)$$

where ψ_t is the solution of the time-dependent Schrödinger equation

$$i\hbar \frac{\partial}{\partial t} \psi_t(\mathbf{x}) = \left(\frac{\hat{\mathbf{p}}^2}{2m_e} + V(\mathbf{x}) \right) \psi_t(\mathbf{x}) \quad (72)$$

with

$$V(\mathbf{x}) = - \sum_j \frac{q_j}{|\mathbf{x} - \mathbf{R}_j|} \quad (73)$$

where the sum is over all protons j , with charge $q_j = +e$, and coordinates \mathbf{R}_j . $\psi_t(\mathbf{x})$ is represented on a three-dimensional grid and propagated according to the standard Split Operator Fourier Transform (SOFT) method.^{40,41} The grid is defined as follows: $x_{\alpha k} = x_{\alpha 0} + k\Delta x$, $k = 1, 2, \dots, 128$, where $\alpha = 1-3$ enumerates the Cartesian directions, $x_{10} = -4$ Å, and $x_{20} = x_{30} = -5$ Å. The grid spacings $\Delta x = 10/128$ Å and $\Delta t = 10^{-4}$ fs define a sufficiently fine space–time grid that ensures an accurate representation of the oscillatory structure of $\psi_t(\mathbf{x})$, even during high-energy collisions (e.g., collisions with tens of electronvolts). The full-quantum propagation is based on the short-time Trotter approximation of the time-evolution operator:

$$\psi_{t+\Delta t}(\mathbf{x}) = U(t, t + \Delta t) \psi_t(\mathbf{x}) \quad (74a)$$

$$\approx e^{-i/\hbar V \Delta t/2} e^{-i/\hbar \hat{\mathbf{p}}^2/2m_e \Delta t} e^{-i/\hbar V \Delta t/2} \psi_t(\mathbf{x}) \quad (74b)$$

The time-evolved semiclassical Wigner distribution $P_t^{\text{SC}}(\mathbf{x}, \mathbf{p})$ is computed as follows:

$$P_t^{\text{SC}}(\mathbf{x}, \mathbf{p}) = (2\pi)^{-3} \int_{-\infty}^{\infty} d\mathbf{s} \int_{-\infty}^{\infty} d\mathbf{p}_0 \int_{-\infty}^{\infty} d\mathbf{x}_0 e^{i(\mathbf{p} - \mathbf{p}_0) \cdot \mathbf{s}} \delta(\mathbf{x}_t - \mathbf{x}) P_0(\mathbf{x}_0, \mathbf{p}_0) \quad (75a)$$

$$= \frac{1}{N} \sum_{j=1}^N \delta(\mathbf{p} - \mathbf{p}_t(j)) \delta(\mathbf{x}_t(j) - \mathbf{x}) \quad (75b)$$

where $\mathbf{x}_t(j)$ and $\mathbf{p}_t(j)$ are coordinates and momenta, obtained by classical KPC propagation. The initial coordinates and momenta

$\mathbf{x}_0(j)$ and $\mathbf{p}_0(j)$ are sampled by Box–Muller Monte Carlo,⁴² using the phase-space distribution $|P_0(\mathbf{x}_0, \mathbf{p}_0)|$.

3.2. Results. Three model systems were analyzed, including electron scattering from a single central proton (model I), scattering from a central proton in the presence of a peripheral proton (model II), and scattering through a cluster of 125 protons in a configuration typical of a high-density plasma (model III). In models I and II, the initial state for the scattering electron was defined according to eq 68, with $\sigma_0 = \sigma = 0.5$ Å, $x_0 = -1$ au, $z_0 = 0$, and $y_0 = k \times 0.2$ au, where $k = 1, 2, \dots, 5$. Therefore, the initial momentum of the scattering electron was defined as follows:

$$\begin{aligned} p_0^2 &= 2m_e \langle T_0 \rangle \\ &= 2m_e (E - \langle V_0 \rangle) \\ &\approx 2m_e \left(E + \frac{1}{r_0} \right) \end{aligned} \quad (76)$$

with $r_0^2 = x_0^2 + y_0^2$, and $E = 9.2$ eV, defining the initial kinetic energies as listed in Table 1.

Figure 2 shows the comparison of electron–proton scattering trajectories, as described by a single classical trajectory (dots, with initial coordinates and momenta defined by the expectation values of the initial state) and the corresponding full-quantum (SOFT, crosses) and Wigner semiclassical expectation values (lines).

Table 1. Impact Parameters y_0 and Initial Kinetic Energies (K.E.) for Trajectories Shown in Figure 2

y_0 (a.u.)	initial K.E. (eV)
0.2	35.9
0.4	34.5
0.6	32.5
0.8	30.4
1.0	28.4

Figure 2 shows that classical trajectories and benchmark full-quantum trajectories agree at very early times but quickly deviate from each other. In contrast, the semiclassical Wigner description is in almost quantitative agreement with full quantum dynamics throughout the whole propagation time for all cases investigated, including model II where scattering trajectories curve away from the central proton due to the significant influence of the peripheral scattering center and the nearly symmetric impact of the central proton on the extended wave packet.

The origin of small deviations, shown in Figure 2, when comparing the Wigner semiclassical description to the full-quantum results, can be traced to the comparison of the distribution functions in configurational space (see Figure 3). The initial (left) and final (right) densities are shown for impact parameter 0.4 Å for models I (top) and II (bottom), respectively. Large dots indicate proton positions, while small dots correspond to the ensemble distribution. Contours are drawn at σ , 2σ , and 3σ from the maximum density integrated over the z coordinate (60.6%, 13.5%, and 1.1%). SOFT (red) density distributions are compared to the semiclassical Wigner distributions (blue), collected in 64^2 quadratic bins covering the quantum grid (i.e., each bin covers 2^3 quantum grid cells). For illustration purposes, the ensemble of trajectories shown in Figure 2 corresponds to a simulation using $5^6 = 15\,625$ trajectories. Contour lines and quantitative measures are derived from simulations using $7^6 = 117\,649$ trajectories. A maximum allowed energy change of 2.72×10^{-2} eV/fs for each trajectory was enforced at each time step as the basis for the adaptive time step, with a smallest allowed time step of 10^{-39} s.

Deviations between SOFT and semiclassical results, shown in Figure 3, include small components of the semiclassical distributions that remain bound, localized at the protons. This is observed even at the final propagation time, although the full quantum distributions have no bound components. This is an intrinsic limitation of the semiclassical Wigner transform picture that becomes even more pronounced for lower energy collisions, when there are more initial conditions bound in the Coulombic

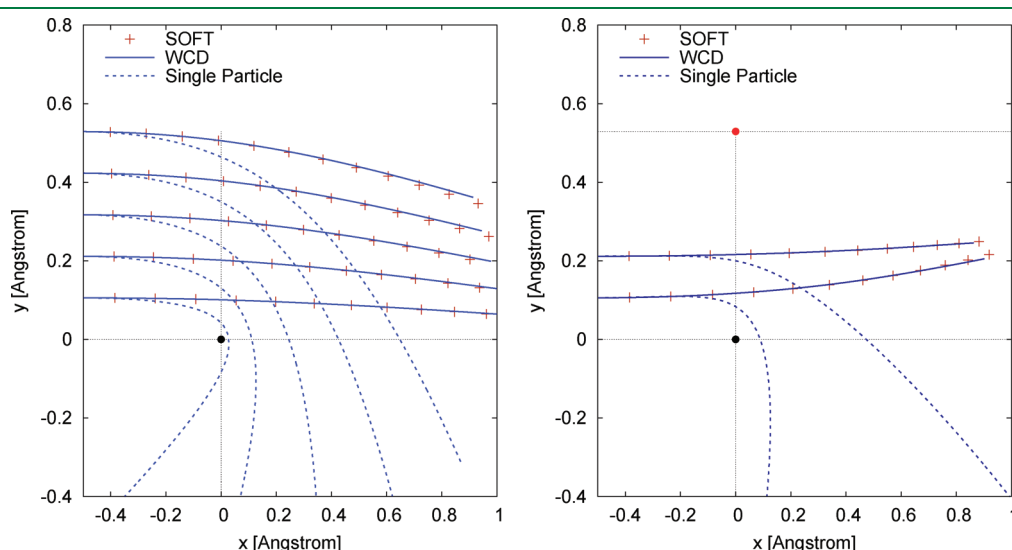


Figure 2. Electron scattering trajectories obtained by expectation values of SOFT full-quantum (red crosses) propagation Wigner classical dynamics (WCD, solid blue) and classical propagation of a single trajectory with initial position and momentum as defined by the expectation values of the initial wave packet (blue dots). Left panel (model I): electron collision with a single proton (black bullet) at the origin. Right panel (model II): collision with two protons, including a central proton at the origin (black bullet) and a peripheral proton (red bullet) at (0,1) au.

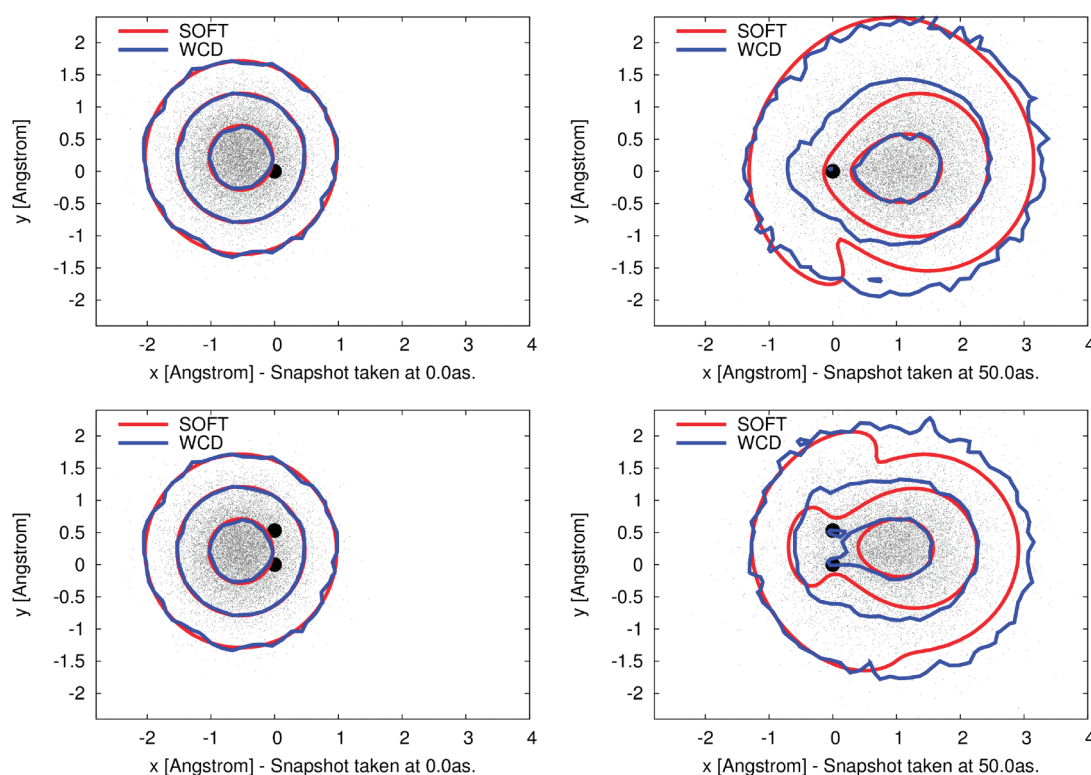


Figure 3. Initial (left) and final (right) densities for impact parameter 0.4 \AA for electron scattering in models I (top) and II (bottom), respectively. Large dots indicate proton positions; small dots are WCD representative configurations. Contours are drawn at percentages of the maximum density (integrated over the z coordinate) found at σ , $2 \times \sigma$, and $3 \times \sigma$ from the center of the distribution, i.e., 60.65%, 13.5%, and 1.1%. Color key: SOFT (red), WCD (blue).

well. As a result, the position predicted by the Wigner transform lags behind the quantum result, faintly visible in Figure 2.

The convex features of the final quantum densities are reproduced well by the WCD method, while concave features in the lowest contour level of the quantum density are due to interference effects and by construction not present in WCD. Nevertheless, the semiclassical Wigner transform reproduces the overall features of the quantum distribution. In fact, a quantitative analysis of the normalized distributions shows $>92\%$ overlap between the semiclassical and quantum distributions for all cases investigated. Even the time-dependent widths, describing the anisotropy of the distribution functions, are in good qualitative agreement with full quantum results.

Figure 4 shows the widths for each of the Cartesian directions describing the time-dependent anisotropy of the distributions. Note that both quantum and semiclassical results show more delocalization along the x direction than in the orthogonal directions y and z . This is likely due to the head-on collision causing the wave packet to undergo more significant deformation in the direction of propagation.

Figure 4 shows that the semiclassical distributions slightly overestimate the widths since they miss interference effects leading to partial localization of the quantum wave packet. This is most prominent in the x direction due to the bound component of the semiclassical distributions, although the trends and overall agreement are quite satisfactory. In fact, close inspection of Figure 3 shows that the semiclassical dynamics reproduce the full-quantum distributions very well, while featuring bound components and deviations at the lowest-density contour level. The concave features in the final quantum density are due to

interference effects, which by construction are not present in WCD. At electron energies above 1 keV, interference becomes negligible, and the agreement of WCD with quantum results becomes excellent. Deviations in the long tails of the distributions, however, affect the overall widths σ disproportionately.

Analogous results are obtained for the description of electron scattering through a cluster of protons (model III). Figure 5 shows the semiclassical (blue) and quantum (red) distributions for a high-energy collision of an electron passing through a disordered cluster of 125 protons (black dots, shown larger for protons closer to the $z = 0$ plane), at the initial (left, $t = 0$ as) and final (right, $t = 50$ as) propagation times. The configuration of the cluster,⁴³ contained in a box with dimensions $5 \times 5 \times 5 \text{ \AA}$, has been extracted from a plasma of density $\rho = 10^{24} \text{ cm}^{-3}$. The initial state for the scattering electron is defined with a width according to a 1s state of a hydrogen atom, and with initial kinetic energy $p_0^2/2m_e = 250 \text{ eV}$.

Numerical Effort. Wall times for production run calculations on a 2.67 GHz intel Core i7 CPU are shown in Table 2. KPC calculations (second column) are compared to results obtained according to the adaptive velocity Verlet method (third column) for two sets of trajectories. The total simulation time is 50 as ($5 \times 10^{-17} \text{ s}$). A maximum of 2^{20} subdivisions of the default time step was allowed, after which a trajectory was marked as failed if it did not satisfy a maximum allowed energy change of $2.72 \times 10^{-2} \text{ eV/fs}$ in one default time step. Trajectories do not fail for the KPC method, while a complete treatment of the failed trajectories in the velocity Verlet method require longer times than given here or are impossible altogether. A larger number of trajectories with randomized initial conditions means an increase

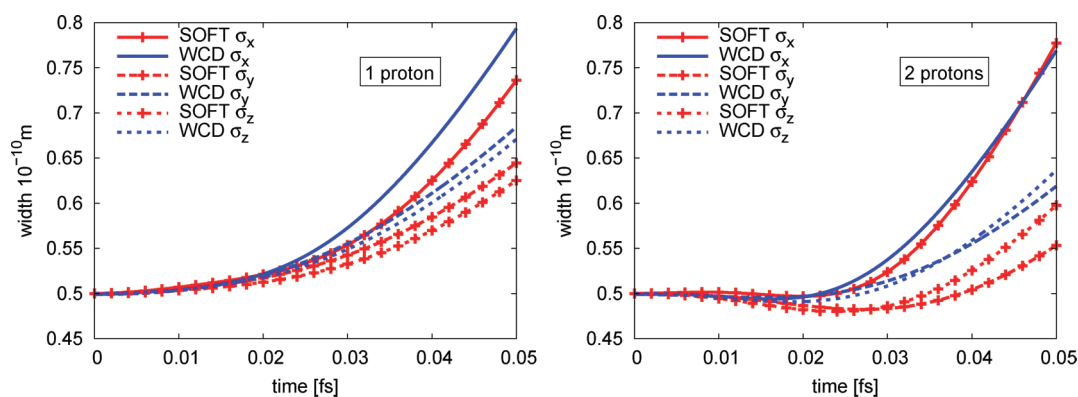


Figure 4. Time dependence of the widths of the time-dependent distributions, as described by semiclassical and quantum calculations of electron scattering in model I (left) and model II (right), respectively. Semiclassical Wigner transforms tend to overestimate the widths, since they lack interference terms responsible for partial localization of the full quantum distributions.

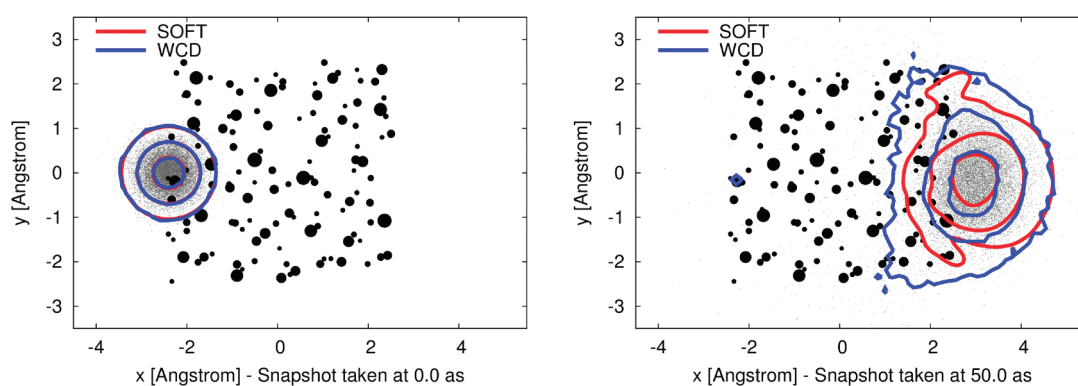


Figure 5. Contour plots of quantum (red) and semiclassical (blue) probability densities, integrated over the z coordinate at the initial (left, $t = 0$ as) and final (right, $t = 50$ as) propagation times, for a high-energy collision of an electron passing through a disordered cluster of 125 protons (black dots, shown larger for protons closer to the $z = 0$ plane). Coordinates x and y in Å.

Table 2. Wall Times for Production Run Calculations (in hours:minutes:seconds) on a 2.67 GHz Intel Core i7 CPU of Adaptive KPC Method with Cutoff (Second Column) and Adaptive Velocity Verlet Method (Third Column) for Two Different Numbers of Trajectories for a Total Simulation Time of $50 \text{ as} \times 10^{-17} \text{ s}$

particles	adaptive KPC	adaptive Verlet	failed KPC trajectories	failed Verlet trajectories
15625	17:25	23:00 (+32%)	0	1 (0.0064%)
117649	1:55:04	2:44:33 (+43%)	0	15 (0.013%)

in the probability of close encounters, which is reflected by the increased ratio between the run times of the two methods and the increased percentage of failed particles.

The selection of trajectories that fail to conserve energy to within $2.72 \times 10^{-2} \text{ eV/fs}$ when propagated according to velocity Verlet are uncontrolled by the user and depend on the dynamics, so that the statistics of the result are skewed. The number of close encounters scales with the third root of the number of particles and linearly with time, making failing trajectories a considerable problem for larger simulations. The adaptive KPC method with cutoffs is more efficient and suffers from no such drawback, so that production runs with 1 million or more trajectories can be performed routinely.

Numerical Accuracy. All KPC results discussed above were performed with an adaptive time step, ensuring that energy conservation is satisfied to a given accuracy. The absence of failed trajectories for the KPC method shows that, time step for time step, the KPC method is more accurate than velocity Verlet and effectively solves the close encounter problem.

To quantify energy conservation, close encounter simulations at a constant time step of a single particle with a resting proton were performed, with a peripheral proton at 1 au distance (model II). Figure 6 shows the energy change of KPC at a constant time step for hyperbolic (left) and elliptic (right) character trajectories. KPC results are shown for cutoff radii of 0.3 au (black lines), 0.2 au (dark gray lines), 0.1 au (light gray lines), and no cutoff, i.e., never using velocity Verlet at any distance (dashed lines). The difficulty of the close encounter is expressed by energy nonconservation caused by it. As the electronic particle approaches the protonic scattering center, the velocity Verlet energy deviates from its initial value, and when switching to the KPC method at the cutoff radius, energy is conserved again before oscillating at the point of closest approach. The energy then returns to the value before its oscillation, before traversing the cutoff radius causes a switch back to velocity Verlet. This demonstrates that, at a given time step, the KPC method conserves energy much closer to the scattering center than velocity Verlet.

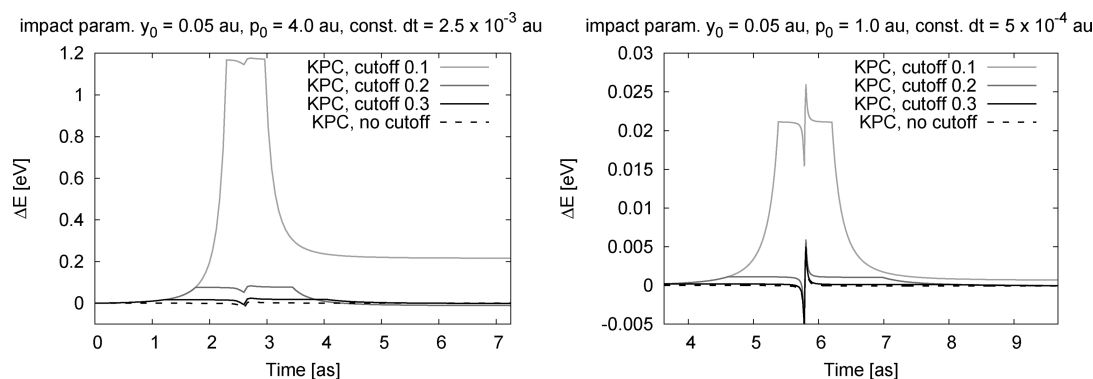


Figure 6. Energy change of KPC at constant time step for hyperbolic (left) and elliptic (right) character trajectories. KPC results are shown for cutoff radii of 0.3 au (black lines), 0.2 au (dark gray lines), 0.1 au (light gray lines), and no cutoff, i.e. never using velocity Verlet at any distance (dashed lines). It can be seen that, approaching the scattering center, the velocity Verlet method shows a significant energy deviation, while switching to KPC causes the energy to level off. Energy nonconservation at the smaller cutoff of 0.1 is due to a break down of the velocity Verlet method already outside the cutoff radius, while using KPC only leads to well conserved energy.

At large cutoff radii, the energy eventually returns to its initial value, demonstrating that the time-reversal symmetric construction of the KPC method solves the close-encounter problem. At the smaller cutoff radius of 0.1 au, the energies do not quite return to their initial value which, considering the success at larger cutoffs, must be ascribed to a break down of the velocity Verlet method already outside the cutoff radius. Velocity Verlet by itself fails at the given time steps, as witnessed by macroscopic energy shifts after the close encounters of 0.30 au (8.3 eV) and 0.55 au (14.9 eV). Note that a shorter time step is shown for the elliptic case, as that leads to a smaller distance of closest approach. For smaller time steps, accuracy is improved, while for larger time steps, the shortcomings of velocity Verlet become more pronounced.

It is worth mentioning that when adaptive time steps are used, smaller cutoff values may be more useful since they allow for a reduction in the numerical effort, which per time step is larger for the KPC method, as well as making sure that cutoff spheres between neighboring protons never overlap, which is why 0.1 au has been used for all adaptive time step Wigner density propagations above. In calculations with many potential wells, where the integrator effort is negligible in comparison to that for evaluation of the potential gradient, a larger cutoff is more useful.

4. DISCUSSION

The KPC method is a highly efficient multipurpose method for simulations of an important class of dynamical problems featuring singular potentials. The method is easy to implement and offers an accurate treatment of dynamical problems in which close encounters between mutually attractive particles may occur. For comparable integration time steps, the KPC method is more accurate than standard integrators, even when the Kepler equation is solved to machine accuracy, since its accuracy is determined by the impact of the slowly varying residual potential on the trajectory (and its occasionally sudden changes of direction). A sample program reproducing the calculations reported in Figure 6 is available free of charge upon request to the corresponding authors.

The KPC method can be made arbitrarily accurate, as opposed to standard integrators which typically break at some finite distance of closest approach when the required time step becomes so small that the operations involved cannot be computed at the given machine accuracy. The cost of the KPC method increases when the distance between singularities decreases,

since the cutoff distance must be reduced to keep it smaller than half the minimal distance between singularities. As the cutoff is reduced, the cost of standard propagation methods, applied outside the cutoff distance, increases.

As presented in this paper, the KPC method is limited to problems with close encounters of two-body collisions. This is usually sufficient for most molecular dynamics simulations where the Coulomb repulsion limits close encounters to pairs of particles of opposite charge and prevents three- and higher-body collisions. The method, however, could still be used in applications to gravitational dynamics where multibody close encounters are much less common than two-body collisions.

To make the KPC method time-reversal symmetric, it has to be made sure that the cutoff distance is crossed during the same default time step in both directions. This is done by observing whether the cutoff is crossed from the inside to the outside during the default time step, reverting back to the underlying numerical integrator if this occurs.

As illustrated for models I–III, the KPC method allows for semiclassical dynamics simulations of phase-space distributions in very good agreement with quantum dynamics simulations. For electron scattering from attractive Coulomb potentials, the KPC approach provides a highly parallelizable approach. The method can be applied in conjunction with a wide range of standard integrators, including high-order predictor corrector methods (such as the Nordsieck–Gear method) since the solution \mathbf{S}^K of the Kepler problem yields also higher time derivatives of the position that can be correctly augmented, as described by eq 25.

At large times, the sampling of classical trajectories becomes an issue, as the dispersion predicted by the Wigner trajectories is limited by the largest momentum among these trajectories. The predictive power of the Wigner density is also easily seen to be limited in its spatial resolution by the number of trajectories employed. In the multiple scattering case, self-interference of the electron may become significant after many interactions, which is not represented by the current method. In the cases presented here, it turns out to play a minor role not significantly altering the resulting densities, so that the Wigner trajectory method yields good agreement with SOFT.

As discussed in previous sections, the KPC method has been implemented and illustrated as applied to modeling single electron scattering from unscreened Coulombic potentials, using

Table 3. Percentage Deviations of the Debye–Hückel Potential and Its Gradient, Relative to the Unscreened Coulomb Potential, for Different Values of Debye Screening Distances and Cutoff Radii

relative deviation	$r = r_{\min}^{\text{Verlet}} = 10^{-2}$ au			$r = r_{\min}^{\text{Gear}} = 10^{-3}$ au		
	$d = 5$ au	$d = 10$ au	$d = 20$ au	$d = 5$ au	$d = 10$ au	$d = 20$ au
$\delta V^{\text{DH}}(r)$	2×10^{-3}	10^{-3}	5×10^{-4}	2×10^{-4}	10^{-4}	5×10^{-5}
$\delta \nabla V^{\text{DH}}(r)$	2×10^{-6}	5×10^{-7}	1.25×10^{-7}	2×10^{-8}	5×10^{-9}	1.25×10^{-9}

a cutoff radius r_{\min} around the scattering centers chosen to optimize accuracy and performance. The multielectron scattering problem becomes rather complicated at low energies due to electron exchange and correlation. Therefore, the Kepler predictor corrector method is expected to be most useful for the description of electron scattering processes at high (keV) energies. In this case, fast electrons may be seen as dressing the nuclear potential seen by an additional electron in the form of the Yukawa, or Debye–Hückel, screened-Coulomb potential:⁴⁴

$$V^{\text{DH}}(r) = \frac{1}{r} \exp\left(-\frac{r}{d}\right) \quad (77)$$

where d is the Debye screening distance. Analogous treatments of KPC can be applied for this and other classes of spherical potentials, especially those whose two-body initial value problem is solved analytically.

The Yukawa potential in particular, however, converges to the Coulomb potential when $r \rightarrow 0$. Therefore, for a sufficiently small r_{\min} , the solution of the unscreened Kepler problem already gives a good approximation to close encounters for the Yukawa potential. The intrinsic error can be minimized by setting r_{\min} to an appropriate value. Table 3 shows how small are the percentage deviations of the Debye–Hückel potential and its gradient, when compared to the unscreened Coulomb potential, for various screening distances d and cutoff radii r_{\min} .

The deviations can be approximated by Taylor expansion of the exponential:

$$\delta V^{\text{DH}}(r) = \frac{V^{\text{DH}}(r) - V^{\text{s}}(r)}{V^{\text{s}}(r)} \approx \frac{r}{d} \quad (78)$$

$$\delta \nabla V^{\text{DH}}(r) = \frac{|\nabla V^{\text{DH}}(r) - \nabla V^{\text{s}}(r)|}{|\nabla V^{\text{s}}(r)|} \approx \frac{1}{2} \left(\frac{r}{d}\right)^2 \quad (79)$$

Through an appropriate choice of r_{\min} , any desired accuracy may be achieved for the KPC method for any given d , with a corresponding impact on computational performance if small r_{\min} values are chosen. Careful analysis of the numerical effort shows that with the Verlet method, a cutoff of 10^{-2} au may be chosen with only minimal penalty to the efficiency of the KPC method. Under ignition conditions, proton density is on the order of 10^{26} cm^{-3} , where the mean distance between protons is larger than 0.2 au, i.e., much larger than this cutoff. If better numerical accuracy is required, efficiency may be traded in to obtain even smaller cutoff distances.

Another class of potentials is the repulsive Coulombic potential between protons, commonly found in high energy density plasma simulations where kinetic energies are sufficiently high as to cause close encounters between protons. As at kiloelectronvolt energies, electron exchange and correlation play a subordinate role for the system's dynamics, the single electron molecular dynamics methods proposed should be applicable. For such simulations, a

repulsive KPC method can be constructed analogously from the analytic solution of the repulsive Kepler problem. For lower energies (the warm dense matter regime), alternative methods taking exchange and correlation into account have to be explored.

5. CONCLUSIONS

We have introduced the KPC algorithm for accurate and efficient simulations of dynamics of particles with attractive $1/r$ singular potentials. When used in its time-reversible form (with a carefully chosen cutoff radius around singularities), the KPC method always reduces the numerical effort with respect to standard integrators and allows for the description of close encounter collisions. The method is easy to implement and should be practical for a wide range of applications where particles gravitate into each other, such as electron–proton interactions and ionic dynamics, as well as applications in other fields with similar computational challenges such as molecular dynamics of high-density plasmas and celestial mechanics.

We have shown how to apply the KPC method to model semiclassical dynamics of electron–proton scattering processes in the Wigner-transform time-dependent picture. The reported results show excellent agreement with benchmark quantum dynamics calculations, including models with multiple scattering centers that defy the capabilities of standard integration methods. The reported results suggest that the Wigner semiclassical dynamics is a practical and accurate approach to include quantum effects in high energy electron–proton collisions when simulated according to the KPC method. The KPC method's applicability to other singular potentials featuring close encounters should provide a useful, easy to implement tool for a wide range of studies, including electron–ion scattering events and particle–antiparticle dynamics, as well as in classical simulations of charged interstellar gas dynamics and gravitational celestial mechanics, where the latter has not been able to profit from KS-regularization.

AUTHOR INFORMATION

Corresponding Author

*E-mail: andreas.markmann@yale.edu; victor.batista@yale.edu.

Notes

The authors declare no competing financial interest.

ACKNOWLEDGMENT

V.S.B. acknowledges supercomputer time from NERSC and support from Lawrence Livermore National Laboratory, grant B590847. The NSF grants CHE-0911520 and ECCS-0404191 supported the development of methods for quantum dynamics simulations. We thank Michael Surh, David Richardson, and Jim Glosli at Lawrence Livermore National Laboratory and Paul Grabowski and Michael Murillo at Los Alamos National Laboratory for valuable comments.

■ REFERENCES

- (1) Jortner, J.; Bixon, M. *Electron Transfer - from Isolated Molecules to Biomolecules*; John Wiley and Sons, Inc.: New York, 1999; pp 1.
- (2) Schwartz, B.; Rossky, P. *J. Chem. Phys.* **1994**, *101*, 6902–6916.
- (3) Turi, L.; Sheu, W.; Rossky, P. *Science* **2005**, *309*, 914–917.
- (4) Harumiya, K.; Kawata, I.; Kono, H.; Fujimura, Y. *J. Chem. Phys.* **2000**, *113*, 8953–8960.
- (5) Dunn, T.; Broyles, A. *Phys. Rev.* **1967**, *157*, 156–166.
- (6) Ashcroft, N. J. *Phys. C: Proc. Phys. Soc.* **1968**, 232–243.
- (7) Turi, L.; Borgis, D. *J. Chem. Phys.* **2002**, *117*, 6186–6195.
- (8) Singh, S.; Kumar, S.; Srivastava, M. *J. Phys. B: Atom. Mol. Phys.* **1978**, *11*, 3061–3066.
- (9) Filinov, A. V.; Golubnychii, V.; Bonitz, M.; Ebeling, W.; Dufty, J. *Phys. Rev. E* **2004**, *70*, 046411.
- (10) Kimura, M.; Inokuti, M. *Phys. Rev. A* **1988**, *38*, 3801–3803.
- (11) Avinash, K.; Eliasson, B.; Shukla, P. *Phys. Lett. A* **2006**, *353*, 105–108.
- (12) Heggie, D.; Hut, P. *The Gravitational Million-Body Problem*; Cambridge University Press: Cambridge, U.K., 2003; p 1.
- (13) Chambers, J. E. *Mon. Not. R. Astron. Soc.* **1999**, *304*, 793–799.
- (14) Heggie, D. *Introduction to stellar dynamics and N-body integrators*. http://manybody.org/modest/heggie_split.pdf (accessed Nov. 2011).
- (15) Paolini, F.; Cabral, E.; dos Santos, A. *36th EPS Conf. Plasma Phys. Sofia* **2009**, *33E*, O-4.039.
- (16) Hernquist, L.; Hut, P.; Makino, J. *Astrophys. J.* **1993**, *402*, L85–L88.
- (17) Kustaanheimo, P.; Stiefel, E. *J. Reine Angew. Math.* **1965**, *218*, 204–219.
- (18) Vivarelli, M. D. *Celest. Mech. Dyn. Astron.* **1985**, *36*, 349–364.
- (19) Neusch, W. *Quaternionic regularisation of perturbed Kepler motion*; Preprint, 1991.
- (20) Aarseth, S. Direct methods for N-body simulations. In *Multiple Time Scales*; Brackbill, J., Cohen, B., Eds.; Academic Press: New York, 1985; pp 377–418.
- (21) Aarseth, S. J. *Gravitational N-Body Simulations*; Cambridge University Press: Cambridge, U.K., 2003; Cambridge monographs on mathematical physics, p 1.
- (22) Aarseth, S. *N-Body Simulation Software*. <http://www.ast.cam.ac.uk/~sverre/> (accessed Nov. 2011).
- (23) Kleppner, D.; Kolenkow, R. J. *An Introduction to Mechanics*, 1st ed.; Cambridge University Press: Cambridge, U.K., 2010; pp 414–416.
- (24) Tuckerman, M.; Martyna, G.; Berne, B. *J. Chem. Phys.* **1990**, *93*, 1287.
- (25) Tuckerman, M.; Berne, B.; Martyna, G. *J. Chem. Phys.* **1992**, *97*, 1990.
- (26) Janezic, D.; Merzel, F. *J. Chem. Inf. Comput. Sci.* **1995**, *35*, 321–32.
- (27) Janezic, D.; Merzel, F. *J. Chem. Inf. Comput. Sci.* **1997**, *37*, 1048–1054.
- (28) Janezic, D.; Praprotnik, M. *Int. J. Quantum Chem.* **2001**, *84*, 2–12.
- (29) Janezic, D.; Praprotnik, M. *J. Chem. Inf. Comput. Sci.* **2003**, *43*, 1922–1927.
- (30) Miyamoto, S.; Kollman, P. A. *J. Comput. Chem.* **1992**, *13*, 952–962.
- (31) Zwicknagel, G.; Toepffer, C.; Reinhard, P.-G. *Phys. Rep.* **1999**, *309*, 117–208.
- (32) Broucke, R. *Astrophys. Space Sci.* **1980**, *72*, 33–53.
- (33) Allen, M. P.; Tildesley, D. J. *Computer Simulation of Liquids*; Oxford Science Publications: Oxford, 1987; p 25.
- (34) Vesely, F. J. *Computational Physics - An Introduction*, 2nd ed.; Kluwer Academic/Plenum Publishers: New York–London, 2001; p 107.
- (35) Swope, W. C.; Andersen, H.; Berens, P. H.; Wilson, K. R. *J. Chem. Phys.* **1982**, *76*, 637–649.
- (36) Condurache, D.; Martinusi, V. *Meccanica* **2007**, *42*, 465–476.
- (37) Odell, A. W.; Gooding, R. H. *Celestial Mechanics* **1986**, *38*, 307–334.
- (38) Gooding, R. H.; Odell, A. W. *Celestial Mechanics* **1988**, *44*, 267–282.
- (39) Wigner, E. *Phys. Rev.* **1932**, *40*, 949–759.
- (40) Feit, M. D.; J. A. Fleck, J.; Steiger, A. *J. Comput. Phys.* **1982**, *47*, 412–433.
- (41) Feit, M. D.; J. A. Fleck, J. *J. Chem. Phys.* **1983**, *78*, 301.
- (42) Box, G.; Muller, M. E. *Ann. Math. Stat.* **1958**, *29*, 610–611.
- (43) Graziani, F. R.; Batista, V. S.; Benedict, L. X.; Castor, J. I.; Chen, H.; Chen, S. N.; Fichtl, C. A.; Glosli, J. N.; Grabowski, P. E.; Graf, A. T.; Hau-Riege, S. P.; Hazi, A. U.; Khairallah, S. A.; Krauss, L.; Langdon, A. B.; London, R. A.; Markmann, A.; Murillo, M. S.; Richards, D. F.; Scott, H. A.; Shepherd, R.; Stanton, L. G.; Streitz, F. H.; Surh, M. P.; Weisheit, J. C.; Whitley, H. D. *High Energy Dens. Phys.* **2011**; DOI: 10.1016/j.hedp.2011.06.010.
- (44) Iafrate, G. J.; Mendelsohn, L. B. *Phys. Rev.* **1969**, *182*, 244–258.